

# Parametrizing the Stellar Haloes of Galaxies

Richard D’Souza<sup>1\*</sup>, Guinevere Kauffman<sup>1</sup>, Jing Wang<sup>1</sup>, Simona Vegetti<sup>1</sup>

<sup>1</sup>Max Planck Institute for Astrophysics, Munich, Germany

Accepted 1988 December 15. Received 1988 December 14; in original form 1988 October 11

## ABSTRACT

We study the stellar haloes of galaxies out to 70–100 kpc as a function of stellar mass and galaxy type by stacking aligned  $r$  and  $g$  band images from a sample of 45508 galaxies from SDSS DR9 in the redshift range  $0.06 \leq z \leq 0.1$  and in the mass range  $10^{10.0} M_{\odot} < M_{*} < 10^{11.4} M_{\odot}$ . We derive surface brightness profiles to a depth of almost  $\mu_r \sim 32 \text{ mag arcsec}^{-2}$ . We find that the ellipticity of the stellar halo is a function of galaxy stellar mass and that the haloes of high concentration ( $C > 2.6$ ) galaxies are more elliptical than those of low concentration ( $C < 2.6$ ) galaxies. The  $g-r$  colour profile of high concentration galaxies reveals that the  $g-r$  colour of the stellar population in the stellar halo is bluer than in the main galaxy, and the colour of the stellar halo is redder for higher mass galaxies. We further demonstrate that the full two-dimensional surface intensity distribution of our galaxy stacks can only be fit through multi-component Sérsic models. Double-Sérsic profiles adequately model the average surface brightness distributions of high concentration galaxies, while triple-Sérsic profiles are often needed to model the surface brightness distributions of low concentration galaxies. Using the fraction of light in the outer component of the models as a proxy for the fraction of accreted stellar light, we show that this fraction is a function of stellar mass and galaxy type. For high concentration galaxies, the fraction of accreted stellar light rises from 30% to 70% for galaxies in the stellar mass range from  $10^{10.0} M_{\odot}$  to  $10^{11.4} M_{\odot}$ . The fraction of accreted light is much smaller in low concentration systems, increasing from 2% to 25% over the same mass range. This work provides important constraints for the theoretical understanding of the formation of stellar haloes of galaxies.

**Key words:** Galaxy Formation – Stellar haloes

## 1 INTRODUCTION

Traditionally, galaxies have been studied through their surface brightness profiles (Hubble 1936; de Vaucouleurs 1948). This has not only revealed a wealth of information about their different morphologies but also hints about their formation processes. De Vaucouleurs (1948) first characterised the surface brightness profiles of giant elliptical galaxies as a simple  $\log I(R) \propto R^{1/4}$  law, which was later also found to fit the bulges of disk galaxies. On the other hand, the disks of spiral galaxies have been traditionally fit with exponential profiles (Freeman 1970). Sérsic (1968) showed that all these profiles are specific cases of a more general  $\log I(R) \propto R^{1/n}$  function, which fits the surface brightness profile of a large number of galaxies from disks to spheroidals, dwarfs, ellipticals and bulges. The shape of the surface brightness profile provides valuable clues about the way in which different galaxies formed.

As deeper and more resolved surface brightness data became available, deviations from these simple laws became clearly evident, indicating that galaxy formation was a more complex process than previously believed (Kormendy et al. 2009). This discovery motivated the use of multiple components to model the surface brightness profiles of galaxies (Kormendy 1977; Simard et al. 2011; Lackner & Gunn 2012). Bulge-disk decompositions helped distinguish pseudo-bulges ( $n \sim 1$ ) from classical bulges ( $n \sim 4$ ). Pseudo-bulges are dense central components of disk galaxies that are flattened and rotationally supported and believed to be built out of disk gas. Classical bulges lie on the fundamental plane linking galaxy size, luminosity and velocity dispersion (Bender, Burstein & Faber 1992).

With the advent of deeper imaging (through Hubble Space Telescope and medium-sized, ground-based telescopes), it has become possible to detect additional fainter stellar structures around both normal galaxies and brightest cluster galaxies (Schweizer 1980; Malin & Carter 1983; Schweizer & Seitzer 1980). Today, stellar haloes of galaxies

\* E-mail address: rdsouza@mpa-garching.mpg.de (RDS)

have been observed and confirmed not only in clusters as intracluster light (ICL), but also in a large variety of field galaxies from early-type to late-type spirals. This is consistent with the idea that the faint stellar halo is built up from the debris of smaller galaxies and satellites that are tidally disrupted (e.g. Bullock & Johnston 2005 and Cooper et al. 2010).

In the Milky Way and in other nearby disk galaxies, the stellar halo and other tidal features have been directly detected through star counts (Bell et al. 2008; Ibata et al. 2014; Monachesi et al. 2013). Observing the stellar halo through star counts is limited to the Local Universe. The integrated light from deep imaging has enabled studies of the stellar haloes of more distant elliptical and spiral galaxies (see e.g. Mihos et al. 2005, Martinez-Delgado et al. 2010, Tal et al. 2009 and van Dokkum et al. 2014). By using modest aperture telescopes (Martinez-Delgado et al. 2010) with innovative telescope design optimised for low surface brightness emission (van Dokkum et al. 2014), one can reduce the systematic errors related to flat fielding and the complex point spread function (PSFs) of the telescope and reach much deeper limiting depths of  $\mu_g \sim 32$  mag arcsec<sup>-2</sup>.

Alternatively, stacking the images of a large number of similar galaxies (e.g. Zibetti et al. 2004, Zibetti et al. 2005, Tal & van Dokkum 2011 and Cooper et al. 2013) enables one to study the average stellar haloes of statistical samples of more distant galaxies. The disadvantage is that information on detailed structure is lost. Zibetti et al. (2004) used stacking techniques to study the stellar haloes of edge-on disk galaxies; Tal & van Dokkum (2011) studied the stellar haloes of luminous red galaxies out to  $z \sim 0.34$ .

Theoretical models (Cooper et al. 2013; Purcell et al. 2007; Oser et al. 2010; Lackner et al. 2012) predict not only large variations between individual stellar haloes of galaxies, but also systematic variations in the average properties of stellar haloes as a function of certain galaxy parameters (for example, halo mass, stellar mass, galaxy bulge-to-disk ratio, etc). In order to constrain theoretical models for the formation of stellar haloes, it is important to study the average properties of the surface brightness profiles of galaxies as a function of these galaxy parameters. In this paper, we stack a large number of galaxy images and study them as a function of stellar mass and galaxy type (late-type or early-type). The SDSS imaging data set is well-suited to study the faint stellar haloes of galaxies (Zibetti et al. 2004, 2005; Tal & van Dokkum 2011). The systematics of stacking many SDSS images to produce a very deep image have been well understood and quantified. This is important because studying low-surface brightness structures is highly dependent on a proper estimation and removal of the sky background. We pay particular attention to the residual sky background obtained after stacking the sky-subtracted images from SDSS DR9. We then model the surface brightness profile of the stacked galaxy including the stellar halo through multi-component fits. We then parametrise the contribution of the stellar halo by deriving the fraction of light in the outer component of the galaxy.

In Section 2, we describe how we select and prepare our galaxy images for stacking. In Section 3, we describe in detail the stacking procedure, our error analysis, PSF analysis and the methodology we employ to derive the ellipticity, surface brightness and the colour profiles for each galaxy stack. In

Section 4, we present the surface brightness and colour as a function of the stellar mass of the galaxy and of galaxy type. In Section 5, we fit models to these surface brightness profiles and determine the fraction of light in the outer faint stellar component. In Section 6, we summarise and in Section 7, we discuss our results in light of our theoretical understanding of the formation of stellar haloes of galaxies. Throughout this paper, we assume a flat  $\Lambda$ CDM cosmology,  $\Omega_m = 0.25$ ,  $\Omega_\Lambda = 0.75$  and Hubble parameter  $h = 0.73$ .

## 2 SAMPLE SELECTION AND IMAGE PREPARATION

We select isolated central galaxies from the MPA-JHU SDSS spectroscopic ‘value-added’ catalogue in the stellar mass range  $10^{10.0} M_\odot < M_* < 10^{11.4} M_\odot$  and in the redshift range  $0.06 \leq z \leq 0.1$ .<sup>1</sup> We apply the isolation criterion outlined in Wang & White (2012): a galaxy of apparent  $r$ -band magnitude  $m_{central}$  is considered isolated if there are no galaxies in the spectroscopic catalogue at a projected radius  $R < 0.5$  Mpc and velocity offset  $|\delta z| < 1000$  km s<sup>-1</sup> with magnitude  $m < m_{central} + 1$ , and none within  $R < 1$  Mpc and  $|\delta z| < 1000$  km s<sup>-1</sup> with  $m < m_{central}$ . We remove all edge-on disk galaxies to avoid adverse PSF effects along the minor axis (de Jong 2008) by choosing only those galaxies with isophotal minor-to-major axis ratio  $b/a > 0.3$ .

We construct mosaics (1200 x 1200 pixels) in the  $g$ ,  $r$  and  $i$  bands centred on each galaxy using the sky-subtracted SDSS Data Release 9 images and **SWarp** (Bertin et al. 2002). Galaxies were removed if found unsuitable for stacking. First, galaxy images with a bright source with an  $r$ -band petrosian magnitude greater than 12.0 and within a distance of 1 Mpc from the centre of the galaxy were removed. Secondly, if the masking algorithm (outlined later) failed due to crowded fields, the galaxy image was discarded. Finally, we calculated a histogram of the difference between each galaxy mosaic after masking and transformation (see later) and the stacked image. Galaxy mosaics lying more than  $5\sigma$  from the mean were discarded. The final sample contains a total of 45508 galaxies.

For our later analysis, we will stack according to stellar mass and concentration. For the stellar mass stacks, we stack galaxies in stellar mass bins of 0.1 dex. For the highest mass bin we stack in a bin size of 0.4 dex. Each stack contains both early and late-type galaxies: late-type galaxies dominate the stacks of lower stellar mass whereas early-type galaxies are predominant at high stellar masses. We can parametrise the shape of the galaxy by using the concentration index  $C = R90/R50$  (where  $R90$  and  $R50$  are the radii containing 90 and 50 per cent of the Petrosian  $r$ -band luminosity of the galaxy). It has been demonstrated that  $C \sim 2.6$  marks the transition from late-type to early-type morphologies (Strateva et al. 2001). In order to study the stellar halo separately for late-type and early-type galaxy morphologies,

<sup>1</sup> The stellar masses used here are as defined by the MPA-JHU catalogue (using a methodology similar to that described in Kauffmann et al. 2003) and corrected for the Hubble parameter  $h = 0.73$ . The stellar mass estimates in the MPA-JHU catalogue were derived from fits to the SDSS fibre photometry and the total **ModelMag** photometry.

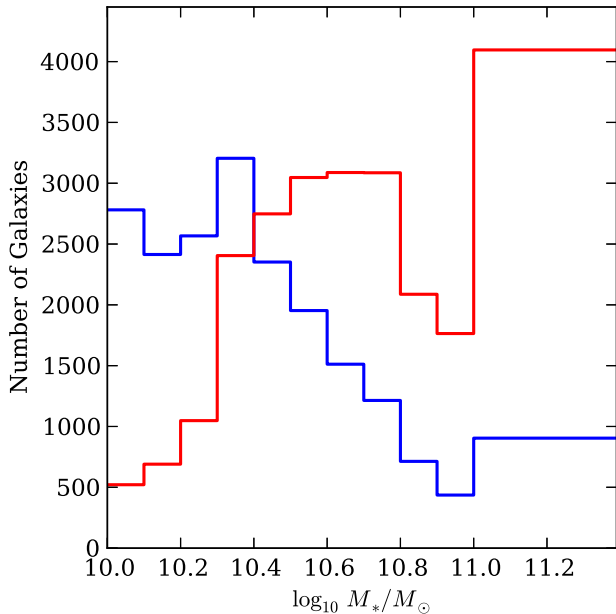


**Figure 1.** The number of galaxies in each mass bin (0.1 dex in width) split according to low concentration ( $C < 2.6$  blue line) and high concentration ( $C > 2.6$  red line) galaxies. The highest mass bin is 0.4 dex in width.

we divide our sample into stellar mass bins of 0.2 dex with a further separation of each stack into high concentration ( $C > 2.6$ ) and low concentration galaxies ( $C < 2.6$ ). The number of galaxies in each stack is displayed visually in Figure 1.

Conservative masking was employed by using multiple runs of **SExtractor** (Bertin & Arnouts 1996) to create segmentation maps. For this purpose, the mosaics of three bands were stacked together to make a ‘master image’, from which several segmentation masks were created to deal with various types of background and overlapping objects. We used a minimum detection area of 5 pixels, a Gaussian filter for detection and a detection threshold of  $1.5\sigma$  to create all the masks. For the background detection, we use three variations. We first calculated the mask with a global background. We then calculate the mask with a local background size of 256 pixels with a filter of 20 pixels. Later we calculated a mask with a smaller background size of 128 pixels with a similar filter size. To deal with extended faint objects, a mask was also created by convolving the master image with an  $8 \times 8$  pixel top hat kernel before running **SExtractor**. Each of these masks were successively applied to individual  $g$  and  $r$ -band mosaics. The  $i$ -band mosaics were only used for creating the master images for the masking procedure.

The masked mosaics were then transformed to  $z = 0.1$  with the flux-conserving IRAF task **GEOTRAN**. This involves both a cosmological surface brightness dimming  $(1+z)^4$  and an image rescaling. For the final transformed mosaic at  $z = 0.1$ , 1 pixel = 0.71 kpc. The mosaics were further cropped to a uniform size of  $950 \times 950$  pixels ( $550 \times 550$  kpc at  $z \sim 0.1$ ) and corrected for Galactic extinction following Schlegel et al. (1998). We ignored  $K$ -corrections in scaling the images as they tend to be minimal at  $z < 0.1$ .

A sizable number of the final transformed images are

oversampled. However, for the redshift shift range chosen for our sample  $z = 0.06 - 0.1$ , this does not significantly affect the noise characteristics of our final transformed images. A final run of **SExtractor** was used to determine the position angle of the galaxy in the  $r$ -band mosaic. This position angle is measured by calculating the second-order moments of the intensity distribution and corresponds to surface brightness threshold  $\mu_r \sim 24 \text{ mag arcsec}^{-2}$ , or a radius of  $\sim 10$  kpc. Each mosaic was then rotated using **GEOTRAN** such that the major axis of each galaxy was aligned.

We note that combining galaxy images into mosaics may introduce additional systematics. Blanton et al. (2011) compared the mosaics created from the sky-subtracted images of DR9 and those created directly from the raw images and found that they yield equivalent results.

The sky subtraction in DR9 (Blanton et al. 2011) is a remarkable improvement from early data releases especially for the extended low surface brightness regions around low-redshift galaxies. Blanton et al. (2011) calculate the residual sky background by measuring the mean surface brightness in random patches of size  $13 \times 13$  native SDSS pixels marked as ‘sky’ in the SDSS pipeline across all imaging runs (see Figure 5 of Blanton et al. 2011). These residuals become significant at depths beyond  $\mu_r \sim 26 \text{ mag arcsec}^{-2}$ . We will discuss this further in the next section.

### 3 IMAGE STACKING AND METHODOLOGY

#### 3.1 Stacking Procedure

Each stack contains between 1000 and 5000 galaxies with an average of 3000 galaxies. The mosaic images in the  $g$  and  $r$  bands were stacked using the IRAF task **IMCOMBINE**, by taking the mean value of each pixel after clipping at the 10th and 90th percentiles.<sup>2</sup> The images were not weighted in the stacking process so as not to bias the sample. The masked parts of the images were not used when calculating the mean value in **IMCOMBINE**. To make the stacking computationally easier, the final stacks were built by combining equal stacks of around  $\sim 100$  galaxy images each. By working in narrow mass bin ranges, we avoid the difficult problem of normalising the size of images in each bin prior to stacking.

#### 3.2 Estimation of Background for Stacked Galaxies

The background ‘sky’ for individual DR9 images consists of the ‘residual’ sky background and light from undetected (unmasked) galaxies. In the Appendix A, we quantify the level of light from undetected sources. This tends to be minimal due to the strict masking procedures employed and the fact that we only select isolated galaxies.

To estimate the residual sky background for the stacked image, we calculate the mean intensity in an annulus between 280 and 320 kpc (400-450 pixels) from the centre of the stacked image. We assume that this background is constant over the whole image. To calculate the uncertainty in

<sup>2</sup> Percentile clipping also helps prune any close satellite galaxies which escape the masking procedure.

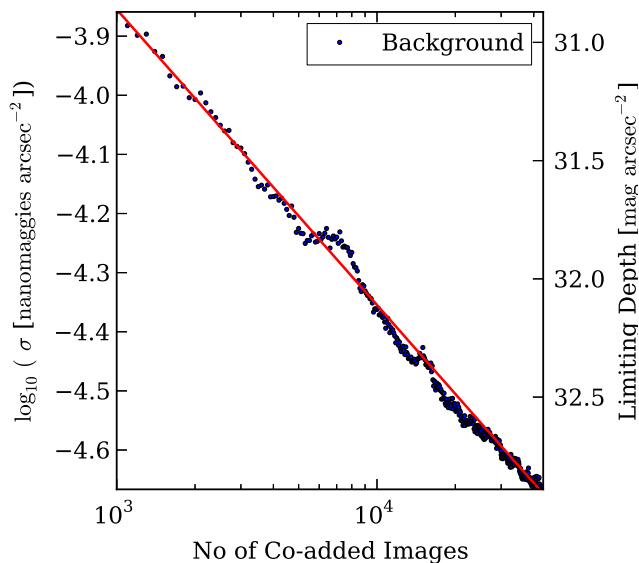


**Figure 2.** The logarithm of the uncertainty in background removal as a function of the number of co-added images. The right axis depicts the limiting surface brightness depth. The red line indicates the function  $0.00442/\sqrt{N_{Images}} \text{nanomaggies arcsec}^{-2}$ .

this background estimation, we calculate the standard deviation of the mean calculated in patches of  $16 \times 16$  pixels within this annulus.

With the standard SDSS imaging, it is possible to extract radial surface brightness profiles down to  $\mu_r \sim 27 \text{ mag arcsec}^{-2}$  (Pohlen & Trujillo 2006). With a better residual background estimation of high S/N stacked DR9 images, it is possible to go significantly deeper. In Figure 2, we plot the uncertainty in the residual background estimation and the corresponding limiting depth in the  $r$ -band as a function of the number of co-added objects. The uncertainty in the residual background estimation can be fit by the function  $0.00442/\sqrt{N_{Images}} \text{nanomaggies arcsec}^{-2}$ .

### 3.3 Error Estimation

For stacks of a few thousand galaxies, the formal uncertainty in the stacked surface brightness profiles at larger radii is dominated by the uncertainty in subtracting the background sky, which consists of camera noise plus extragalactic background radiation originating in the stellar populations of galaxies at moderate to high redshift. These uncertainties calculated as described in the previous section are depicted as solid error bars in the plots discussed in the next section. In addition to the uncertainty that arises from the sky subtraction, it is interesting to consider the variance that arises from the fact that similar galaxies may have stellar haloes with quite different masses and sizes. This can be quantified for each pixel in our final  $g$  and  $r$  band stacks through a bootstrapping procedure. For each bin, 3000 stacks were created with repetition and the variance in each pixel is calculated for each band. This gives the total uncertainty of each pixel. After accounting for the formal uncertainty, the

variance in the surface brightness profiles can be calculated and is depicted as shaded regions in the plots.

To verify that the faint outer stellar halo visible in our stacks between  $30 - 32 \text{ mag arcsec}^{-2}$  is not a product of systematics in the data or due to our stacking procedure, we created equivalent background stacks (nearly 3000 images) for each bin by choosing a location 5 Mpc away from the centre of the galaxy in a random direction where no large galaxies were found within a distance of  $1 \times 1$  Mpc. We found that evaluating the background at these very large distances made no difference to our results.

### 3.4 PSF Effects

The PSF flattens the ellipticity and the surface brightness profiles at the centre of the galaxy at radii less than  $\sim 10$  kpc. For deep images, the light in the faint outskirts of the stack can be dominated by the scattered light from the centre of the galaxy. Failure to account for the difference in the extended wings of the PSF, especially in the  $i$ -band, can lead to a reddening of the colour of the stellar halo (de Jong 2008). This is very visible along the minor axis of edge-on disk galaxies where the surface brightness decreases faster than the profile of the wings of the PSF.

We choose not to deconvolve the stacked galaxy profiles. The effect of the PSF is much smaller in our work than that of Tal & van Dokkum (2011) due to the fact that the galaxies are much closer in redshift. For data interpretation purposes, we will model the two-dimensional stacked image of the galaxy convolved with the average PSF. We have thus constructed average PSF stacks in the  $g$ ,  $r$  and  $i$  bands by combining the synthetic PSFs created using Robert Lupton’s Read Atlas Images code<sup>3</sup> and stacked bright star images according to the procedure outlined in Tal & van Dokkum (2011). The PSF profiles for the  $g$ ,  $r$  and  $i$  bands are shown in Figure 5.

Due to the fact that the PSFs in the  $g$  and in the  $r$ -bands are similar (see also Fig 2 of de Jong 2008 as well as Fig 6 of Bergvall et al. 2010), our  $g$ - $r$  colour profiles are not significantly affected by PSF effects, especially in the outer parts of the profiles. However, the  $i$ -band PSF does differ significantly (see Figure 5) in having wings that extend to much larger distances. We therefore avoid the use of the SDSS  $i$ -band.

### 3.5 Ellipticity, Surface Brightness and Colour Profiles

Measuring the ellipticity can help quantify the shape of the average stellar halo. The ellipticity profiles  $(1 - b/a)$  for each of the aligned galaxy stacks are determined by generating intensity contours at various distances from the centre of the stacked image of the galaxies in the  $r$ -band. For deriving contours which were greater than 20 pixels away from the centre of the galaxy stack, we smooth the image with a Gaussian filter with a width of 3 pixels. For contours beyond 60 pixels from the centre of the galaxy stack, we smooth the image with a larger Gaussian filter (width of 5 pixels).

In Figure 3, we plot ellipticity profiles out to radii of

<sup>3</sup> [http://www.sdss.org/DR7/products/images/read\\_psf.html](http://www.sdss.org/DR7/products/images/read_psf.html)

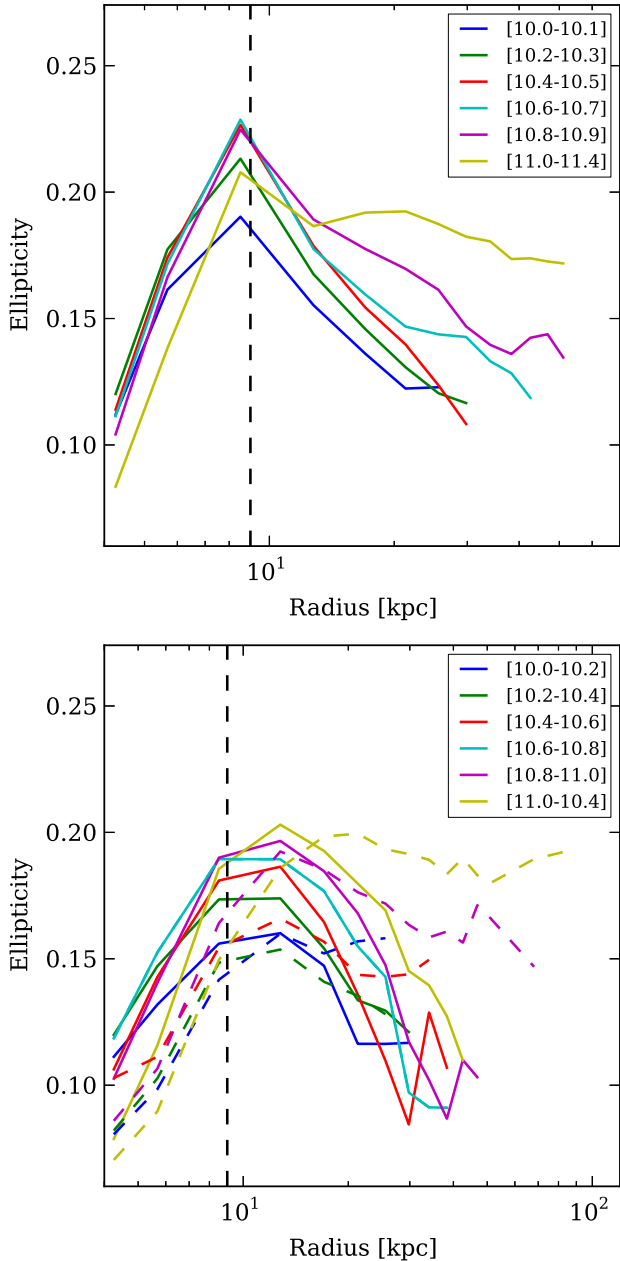


**Figure 3.** (a) Ellipticity profiles for successive stellar mass bins. (b) Ellipticity profiles for each of the stellar mass bins divided according to concentration. Solid lines and dashed lines indicated low ( $C < 2.6$ ) and high ( $C > 2.6$ ) concentration galaxies respectively. The vertical dashed line indicates the maximum radius affected by the PSF.

30-50 kpc for our stacks divided according to stellar mass and concentration. Information on the shape of stellar haloes can be inferred from the average ellipticity profiles for each stack. Only the inner part ( $< 10$  kpc) of the ellipticity profile is significantly affected by the PSF. The outer parts of the ellipticity profile show a gradual change in ellipticity with radius. The ellipticity profile of the stacks of lower stellar mass decreases as the radius increases, i.e. for these galaxies the outer part of the stellar halo is more circular than the inner part of the galaxy. The ellipticity of the outer part of the

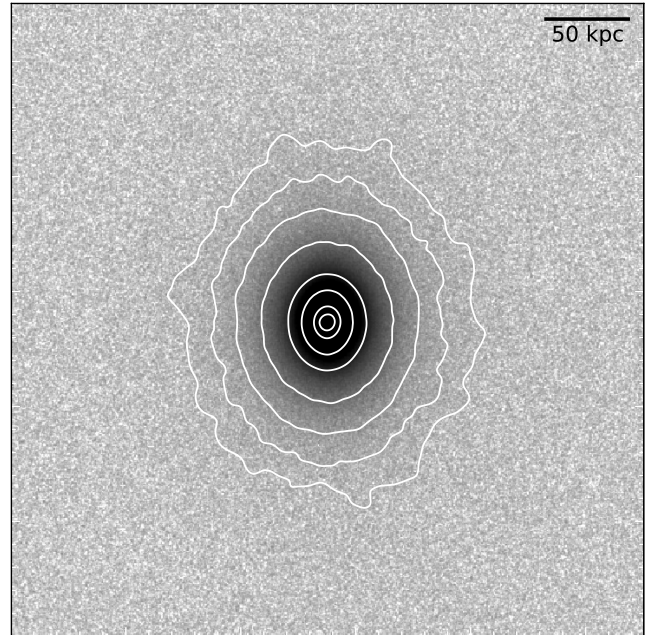


**Figure 4.** The stacked image consisting of 4040 images in the mass range  $10^{11.0} M_{\odot} < M_{*} < 10^{11.4} M_{\odot}$  and  $C > 2.6$ . Elliptical contours are drawn at 5, 10, 20, 30, 50, 70, 90 and 110 kpc.

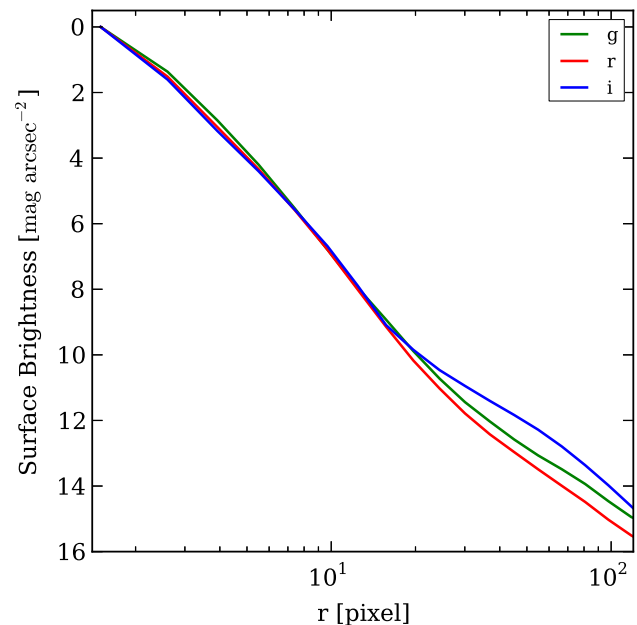


**Figure 5.** SDSS Point Spread Functions colour coded for the  $g$ ,  $r$  and  $i$  bands as indicated by the legend.

stellar halo increases as a function of  $M_{*}$ . The highest stellar mass bins have a maximum outer ellipticity of  $\sim 0.17$ , which remains approximately constant from 30 to 50 kpc. In Figure 4, we show the stacked image of high concentration galaxies stacked in the mass range  $10^{11.0} M_{\odot} < M_{*} < 10^{11.4} M_{\odot}$  along with elliptical contours drawn at various radii.

We find that the stellar haloes of low concentration galaxies tend to be spherical, while the stellar haloes of high concentration galaxies tend to be elliptical. At fixed mass,

the ellipticity of the highest stellar mass, high concentration galaxies reaches values of 0.2 and is approximately constant from 20 to 100 kpc. By contrast, the measured ellipticity ( $1 - b/a$ ) of low concentration galaxies is around 0.1.

Are these results consistent with other measurements? The stellar halo of M31 can easily be measured out to large distances and is found to be nearly spherical (Ibata et al. 2014). At 80 kpc for high concentration high stellar mass galaxies, the measured ellipticity is  $0.21 \pm 0.08$ . This is also consistent with the ellipticity of the stellar halo of LRGs measured by Tal & van Dokkum (2011) which lies around  $\sim 0.25 - 0.3$ . On the other hand, Sesar (2011) measured the axial ratio of the Milky Way stellar halo out to a distance of 35 kpc and estimated it as  $q \sim 0.7$ , i.e. an ellipticity of 0.3, which lies outside the range spanned by our estimates. This may imply that the Milky Way’s halo is unusual. We note, however, that when stacking aligned galaxies together, we assume that the outer stellar halo is also aligned with the shape of the galaxy. If this were not the case, it would lead to a systematic uncertainty in the intrinsic ellipticity which would increase with radius. As a result, the ellipticity measured is a lower limit on the true average intrinsic ellipticities of the stellar haloes of the galaxies which make up the stack. Convolution of the stacked images creates additional measurement uncertainties.

Using these ellipticity profiles, we derive surface brightness in the  $r$  band and  $g-r$  colour profiles in elliptical annuli after background subtraction. At radii where the ellipticity estimates are no longer reliable, we assume that the ellipticity profile flattens out at the furthest determined value of the ellipticity.

## 4 ANALYSIS OF STACKED IMAGES

### 4.1 Profiles in Stellar Mass Bins

In Figure 6, we show the average surface brightness profiles and the average  $g-r$  colour profiles for our galaxy stacks in stellar mass bins. The surface brightness profiles extend reliably to a depth of  $\mu_r \sim 32$  mag arcsec $^{-2}$ . The profiles of highest mass bins reach out to 100-150 kpc, while the lower mass bins extend up to 60-100 kpc. The surface brightness profile of the stellar halo show variations with stellar mass. As discussed in Cooper et al. (2013), the trend in the surface brightness profiles in the stellar mass range  $10^{10.7} M_\odot < M_* < 10^{11.4} M_\odot$  is consistent with the theoretical predictions. In this paper, we extend the analysis down to  $10^{10} M_\odot$ ; comparison with model predictions will form the subject of a future paper.

The triangle markers in the colour profiles indicate the average  $R50$  (the radius enclosing 50 per cent of the Petrosian  $r$ -band luminosity of the galaxy) for each mass bin. For each mass bin, there is a flattening in the colour profile and a hint of an upturn beyond the average  $R50$  indicating that we may be seeing the effects of an older accreted component. We will quantify this in more detail in the next section.

### 4.2 Profiles in Stellar Mass Bins divided by Concentration

In Figure 7, we show the average surface brightness profile and the average  $g-r$  colour profiles for our galaxy stacks separated into high ( $C > 2.6$ ) and low ( $C < 2.6$ ) concentration galaxies.

The surface brightness profiles reveal a clear difference in the shapes of the stellar haloes of high concentration and low concentration galaxies. We can parametrise the shape of the stellar halo by measuring its outer slope. The outer slope is measured through a Bayesian methodology that takes into consideration the scatter due to the variance of the shape of the surface brightness profile of the galaxy. The details are outlined in Appendix B.

In Figure 8, we plot the slope  $\Gamma = d(\log_{10} I)/d(\log_{10} R)$  beyond 25 kpc of the surface brightness profile as a function of stellar mass and galaxy type. At these radii, the surface brightness profiles are not significantly affected by the PSF. The error bars include the variance of the shape of the surface brightness profile of the galaxies in the stack estimated through bootstrapping. For low concentration galaxies, the outer slope steepens from  $\Gamma \sim -2.5$  at low stellar masses to  $\Gamma \sim -4.4$  at higher stellar masses. For high concentration galaxies, the outer slope steepens from  $\Gamma \sim -2.3$  at low stellar masses to  $\Gamma \sim -3$  at higher stellar masses. At fixed mass, the outer slopes of the profiles of low concentration galaxies are steeper than those of high concentration galaxies. The variance in the slope is much larger for low concentration than high concentration galaxies. Similarly the variance in the slope is much larger for low-mass than high-mass galaxies.

Ibata et al. (2014) analyze the power-law slope of the two-dimensional projected distribution of star counts in M31 and find  $\Gamma = -2.30 \pm 0.02$ . We again caution the reader that in stacking large number of galaxies together with different concentrations, the resulting outer slope is a linear combination of the outer slopes of the individual galaxies which go into the stack, so our results are not directly comparable to those obtained for individual galaxies.

### 4.3 Colour Profiles as a function of Stellar Mass and Concentration

The  $g-r$  colour profiles extend out to 15-35 kpc for low concentration galaxies and up to 40-70 kpc for high concentration galaxies. There also appears to be a clear separation between the inner ( $R < 10$  kpc) colour profiles, where  $g-r$  decreases as a function of radius, to a region where colour remains more constant. This is seen for both low and high concentration galaxies. Low concentration galaxies show steeper inner colour gradients than high concentration galaxies. The colour gradient is also steeper in low concentration galaxies with high stellar masses than in low concentration galaxies with low masses (See also Gonzalez-Perez, Castander & Kauffmann 2011, Tortora et al. 2010 and Suh et al. 2010).

For low concentration galaxies, there appears to be a minimum in the  $g-r$  colour beyond which the colour profiles redden. This minimum occurs between 10 kpc for low mass galaxies and 20 kpc for higher mass systems. For high concentration galaxies, the colour profiles flatten, but do not exhibit a pronounced upturn. This is consistent with the

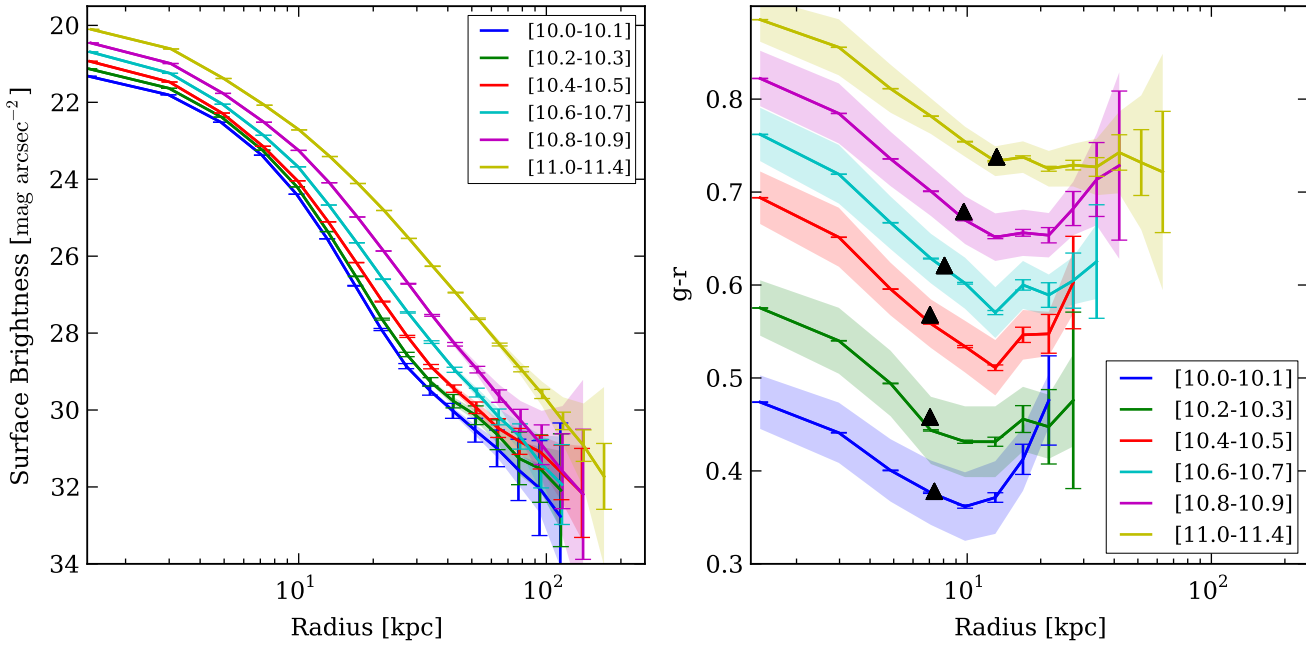


**Figure 6.** Surface brightness profiles and  $g-r$  colour profiles of stacks for successive stellar mass bins. The error-bars show the sum of instrumental errors and uncertainty in background subtraction, while the shaded regions show the spread due to the variation in the shape of the stellar halo. The triangles in the colour profiles mark the average R50 of galaxies in the respective bin.

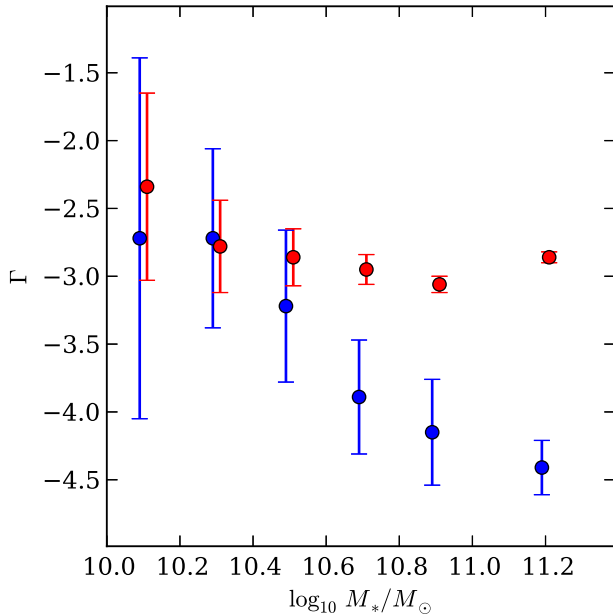


**Figure 8.** The slope  $\Gamma = d(\log_{10} I)/d(\log_{10} R)$  of the surface brightness profile beyond 25 kpc. Blue represents low concentration galaxies, while red represents high concentration galaxies. The errors represent the total variance in the slope of the surface brightness profile estimated from bootstrapping the samples in the stack.

flattening in colour profiles detected in LRGs (Tal & van Dokkum 2011). Reddening of the colour profile at large radii cannot be attributed either to the difference in the PSF in the  $g$  and  $r$  bands or due to the errors in the background

subtraction. The colour profiles of low concentration galaxies do not probe the area where the stellar halo becomes dominant. Bakos et al. (2008) have shown that 90% of the light profiles of the disks of late-type galaxies exhibit deviations from a pure exponential either as truncations (60%) or as anti-truncations (30%). The colour profiles of disks with truncations are “U-shaped”. Disks with anti-truncations exhibit a plateau in  $g-r$  colour at large radii. When stacking a large number of low concentration galaxies together containing with a minimum or a flattening in the  $g-r$  colour profile, the combined effect results in behaviour intermediate between the two. Deeper data is required to probe the colours of stellar populations in the stellar halo. Monachesi et al. (2013) detect a flattening of the colour profile of the stellar halo of M81.

The presence of bluer colours in the outer end of both low and high concentration galaxies as compared to the centre of the galaxy may indicate the presence of stars with significantly younger populations in these outer parts. However, it will be difficult to confirm this without being able to break the degeneracy between age and metallicity by using colours that involve either the  $i$  or  $z$  bands.

We plot the  $g-r$  colour gradient  $\nabla_{g-r} = \frac{\Delta(g-r)}{\Delta(\log R)}$  for our galaxy stacks in Figure 9. For low concentration galaxies, we evaluate the slope for the path of the steepest descent interior to the minimum in the  $g-r$  colour profile. For high concentration galaxies, the slope is derived for the steepest descent interior to the point where the  $g-r$  colour profile flattens. Since the colour profile is affected by the PSF at the centre of the galaxy stack, the analysis is restricted to radii beyond 3 kpc. The gradient is first evaluated from 3 kpc right up to the minimum in the  $g-r$  colour profile, and the path length over which the gradient is calculated is decreased step-by-step until the gradient reaches its maxi-

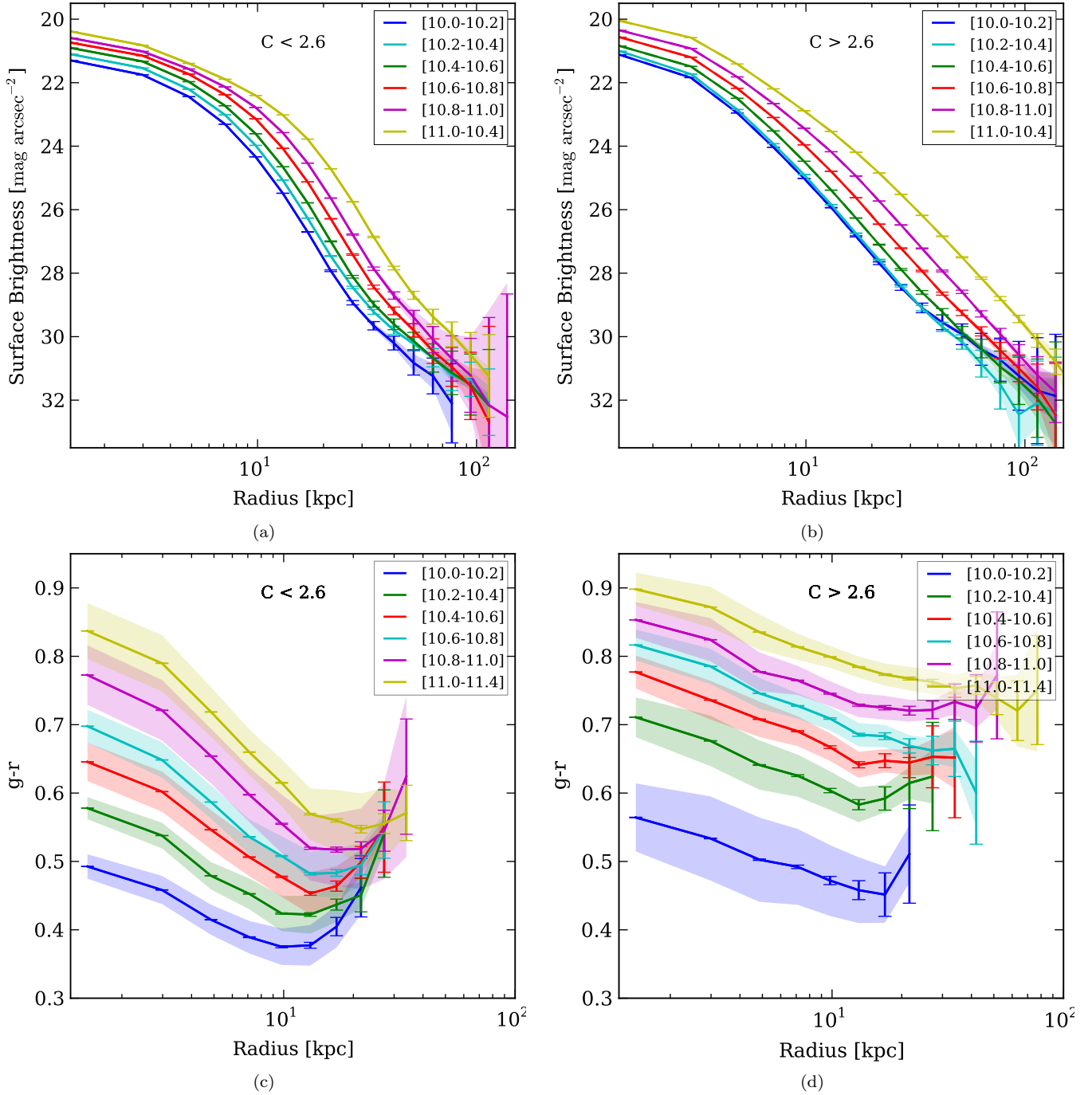


**Figure 7.** Surface brightness and  $g-r$  colour profiles of the stellar mass bins divided according to concentration. The error-bars show the sum of the instrumental errors and the uncertainty in background subtraction, while the shaded regions show the spread due to the variation in the shape of the stellar halo.

mum. Figure 9 shows that colour gradients are stronger in late-type galaxies than in early-type galaxies. In early-type galaxies, the gradients do not depend on stellar mass, but in late-type galaxies, high mass galaxies have much steeper gradients than low mass galaxies.

## 5 MULTI-COMPONENT MODELLING OF THE GALAXY

For each stacked image, we model the full two dimensional  $r$ -band intensity distribution of the galaxy stack using multi-component Sérsic models. We are particularly interested in modelling the outer stellar halo light of the galaxy and in placing constraints on the amount of accreted stellar material. We are confident that the depth of our stacked images means that we can reach out into the extended stellar halo

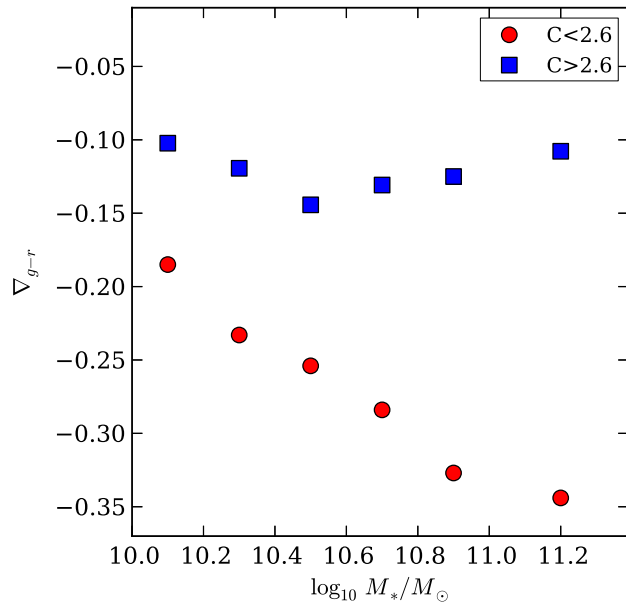


**Figure 9.** The gradient in the  $g-r$  colour profile,  $\nabla_{g-r} = \frac{\Delta(g-r)}{\Delta(\log_{10} R)}$ , measured along the path of the steepest descent for low concentration galaxies interior to the radius where the profile exhibits an upturn, and for high concentration galaxies interior radius where the colour profile flattens.

of the galaxy. Theoretical considerations indicate that there should be an inflexion or a change in the surface brightness profile of the galaxy where the accreted stellar component begins to dominate (Cooper et al. 2013).

The Sérsic (1968) profile  $\log I(r) \propto r^{1/n}$  is the most versatile among the models and is traditionally used to fit the surface brightness profile of galaxies. The Sérsic profile reduces to an exponential ( $n = 1$ ) profile for disk galaxies, while  $n = 4$  profiles (de Vaucouleurs 1948) has been used to model bulges and ellipticals. Kormendy et al. (2009) have demonstrated that the Sérsic profile fits elliptical galaxies and spheroidals very well over a large dynamic range in radius. They also suggested that departures from these profiles could provide new insights into galaxy formation. In this paper, we leave aside the issue of departures from the Sérsic profile at small radii in our galaxy stacks. Our aim is to explore our ansatz that the excess light (deviations from the single Sérsic profile) detected at large radii ( $R > 20$  kpc) is indicative of additional components in the galaxy, which may be attributed to accreted stellar material. Our second ansatz is that the radial variation of ellipticity can also be indicative of various galaxy formation processes. In particular, the difference in ellipticity between the inner part of the galaxy and the outer stellar halo of the galaxy may yield clues to the origin of these components.

Deviations from simple profiles at large radii and the radial variation in ellipticity can be adequately modelled through multi-component modelling, where each component can be represented by a Sérsic profile with a fixed ellipticity. The flexibility of the Sérsic profile helps us model a large variety of possible profiles. The real challenge of modelling galaxies is in assigning a physical significance to each of these components. In fitting multiple components to our galaxy

stacks, we are motivated by the results of Cooper et al. (2013) who have demonstrated theoretically from particle-tagging methods that the in-situ and the accreted surface density profiles are well fit by Sérsic (1968) functions, while the total profile is best fit by a sum of these two functions.

We seek to model the two-dimensional intensity profile of the galaxy with a minimum number of components. In the following subsections, we model separately the stacks of high concentration and low concentration galaxies. We first show that a single component is not sufficient to model the surface brightness profile of high concentration galaxies. We demonstrate how the surface brightness profile of high concentration galaxies can be successfully modelled by two components. For low concentration galaxies, we show that we may need three components to model the disk breaks of galaxies in addition to the stellar halo. For all our fitting procedures, we use the full two-dimensional information in the stacked image. We also test our modelling on mock images of high and low concentration galaxies.

### 5.1 High Concentration Galaxies

High concentration galaxies are simpler to model than low concentration galaxies. Motivated by this, we first fit a single two-dimensional Sérsic model with a fixed ellipticity to our high concentration galaxy stack:

$$I(R) = I_0 \exp \left\{ -b_n \left( \left( \frac{R(q)}{R_e} \right)^{1/n} - 1 \right) \right\}, \quad (1)$$

where  $I_e$  is the intensity at the effective radius  $R_e$  that encloses half of the total light from the model and  $n$  is the Sérsic index. The constant  $b_n$  is defined in terms of the Sérsic index. The radial distance,  $R$ , is a function of the Cartesian coordinates and the ellipticity  $q$  of the model. We also model an additional constant sky component. A single Sérsic model so defined has a total of 4 free parameters.

We compare this with a double Sérsic model with a common centre and with different ellipticities for each Sérsic component. Sérsic profiles extend out to infinity. In order to ensure that the outer stellar halo is determined by only one component, we smoothly cut off the inner Sérsic profile at large radii: the surface brightness profile is suppressed beyond  $7R_{eff}$  and drops to zero outside  $8R_{eff}$ .<sup>4</sup> With an additional constant sky component ( $c$ ), the double Sérsic model has a total of 9 free parameters. There are two additional free parameters for the centre of each model. To reduce the number of free parameters, we determine and fix the centre of the galaxy stack by fitting a single Sérsic model with variable parameters for the centre. All the models considered are symmetric along the major axis and the minor axis. The asymmetries in the image (in the form of bars, bulges, disks, pseudo-bulges, etc.) are not explicitly modelled and appear as residuals.

For the fitting procedure, each model was convolved with the average stacked SDSS PSF before fitting (see section 3.4). We employ a Bayesian technique with uniform and physical priors for all the parameters  $\theta$  ( $I_0 : 0-$

<sup>4</sup> The same procedure is followed in SDSS for pure de Vaucouleurs profile to calculate `ModelMag`.

1 nanomaggies arcsec<sup>-2</sup>;  $R_e$  : 1–100 pixels;  $n$  : 0–10;  $c$  : 0–1 nanomaggies arcsec<sup>-2</sup>;  $q$  : 0–10).

Applying Bayes’ theorem, we can find the posterior probability distribution over the parameters  $\theta$  as

$$p(\theta | \mathbf{D}) = \frac{p(\mathbf{D} | \theta)}{\int_{\theta} p(\mathbf{D} | \theta)p(\theta) d\theta} \cdot p(\theta), \quad (2)$$

where  $\int_{\theta} p(\mathbf{D} | \theta)p(\theta) d\theta$  is the model evidence and  $\mathbf{D}$  is the data.

$p(\mathbf{D} | \theta)$  is the likelihood which can be constructed as follows:

$$\log(L) = -\frac{1}{2} \log((2\pi)^k \Sigma) - \frac{1}{2} (\mathbf{D} - \mu(\theta))^T \Sigma^{-1} (\mathbf{D} - \mu(\theta)), \quad (3)$$

where  $\Sigma$  is the covariance matrix (which is diagonal in this case),  $\mathbf{D}$  is the stacked data,  $\mu$  is the model as a function of the parameters  $\theta$  and  $k$  is the number of independent pixels.

We use MULTINEST (Feroz, Hobson & Bridges 2008; Feroz et al. 2013), a Bayesian inference tool on the full stacked image. This has the advantage over Galfit (Peng et al. 2010) in that it can explore the complete parameter space. We use the full image  $950 \times 950$  pixels for the fitting procedure. This is essential for a proper determination of the residual sky component in the stacked images. In general, the determination of the outer Sérsic index is correlated with the sky component.

We generate a full posterior probability distribution function (PDF) of all the parameters using MULTINEST. This allows us to evaluate the degeneracies in the parameters. If the posterior PDF is double modal (i.e., contains two maxima), we choose the most physical model such that the effective intensity ( $I_e$ ) / effective radius ( $R_e$ ) of the inner most component should be larger/smaller than that of the outer component. For the final parameters of the model, we use the mean values of the posterior PDF. These mean values automatically encode information on the parameter degeneracies.

To compare the various models with each other, we can use two approaches. The first involves using the Bayesian “evidence” marginalised over the model parameters for model comparison. This compares models on a global scale. On the other hand, comparing residuals (or the reduced chi-square) in specific regions of the stacked image allows one to judge the goodness of fit for specific components of the galaxy stack including the stellar halo.

To compare models globally, we construct the Bayes factor ( $B_{10}$  - hypothesis 1 over hypothesis 0). Kass and Raftery (1995, Journal of American Statistical Association) suggest comparing  $2 \log_e(B_{10})$  and note that a factor  $> 10$  is indicative of strong evidence against hypothesis 0. The square root of  $2 \log_e(B_{10})$  gives us the level of significance between the two models. We compare the factor  $2 \log_e(B_{D/S})$  which is comparing the double Sérsic model over the single Sérsic model for a range of mass bins in Table 1. In Figure 11, we show how well the double Sérsic model fits the surface brightness profiles for a range of stellar mass bins.

In Figure 10, we compare the single-Sérsic and double-Sérsic models for the high concentration galaxy stack in the highest stellar mass bin  $10^{11.0} M_{\odot} < M_* < 10^{11.4} M_{\odot}$ . The single-Sérsic function fits the symmetric central high S/N part of the surface brightness profile up to a surface brightness of  $\mu_r \sim 27$  mag arcsec<sup>-2</sup> reaching out to 30 kpc.

**Table 1.** We compare the double-Sérsic model with the single-Sérsic model by comparing  $2 \log_e(B_{D/S})$ , where  $B_{D/S}$  is the Bayes factor favouring the double-Sérsic model over the single-Sérsic model

Mass bin	$2 \log_e(B_{D/S})$
10.0-10.2	3713
10.2-10.4	9779
10.4-10.6	23508
10.6-10.8	30831
10.8-11.0	21730
11.0-11.4	18727

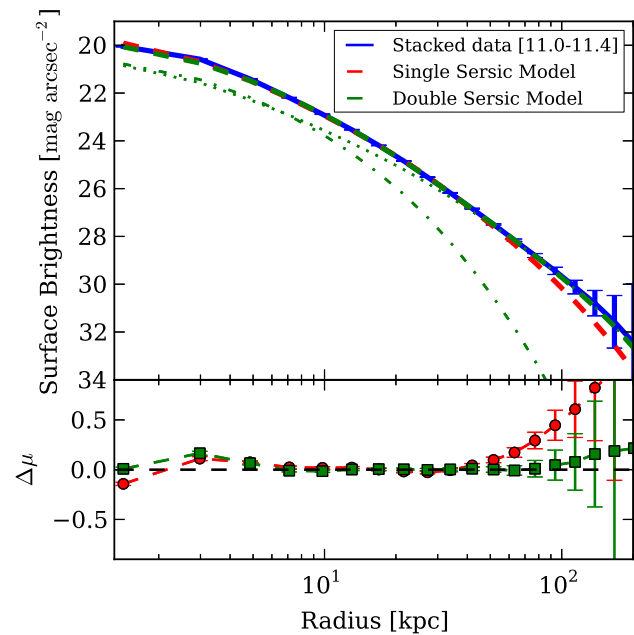


**Figure 10.** Comparison of the the double-Sérsic (dashed green) and the single-Sérsic (dashed red) models with the surface brightness profile of the high concentration highest stellar mass bin stack  $C > 2.6, 10^{11.0} M_{\odot} < M_* < 10^{11.4} M_{\odot}$ ). For the double-Sérsic model, the internal component is denoted by the dot-dashed line while the outer component is denoted by the dotted line.

Note that all internal galaxy components (e.g. bulges, disks, pseudo-bulges) are averaged out and incorporated into the single-Sérsic fit. Beyond 30 kpc, excess light is detected. The double-Sérsic profile on the other hand provides an excellent fit up to a depth of  $\mu_r \sim 32$  mag arcsec<sup>-2</sup> reaching out to 130 kpc. The residuals are shown in the panel below in Figure 10. The residuals of the double-Sérsic are less than 0.2 mag arcsec<sup>-2</sup> across the whole radial range (0–120 kpc) of the galaxy stack. The residuals at the centre are attributed to the asymmetric part of the intensity distribution at centre of the galaxy stack due to the various internal galaxy components mentioned above.

We find that the double-Sérsic profile provides a much better fit for all high concentration galaxies across all mass bin ranges. This can be seen visually by calculating and comparing the residuals of the image beyond 20 kpc for each model. Significant deviations are only seen in the lower two mass bins. The fits to the lowest mass bin is not perfect due

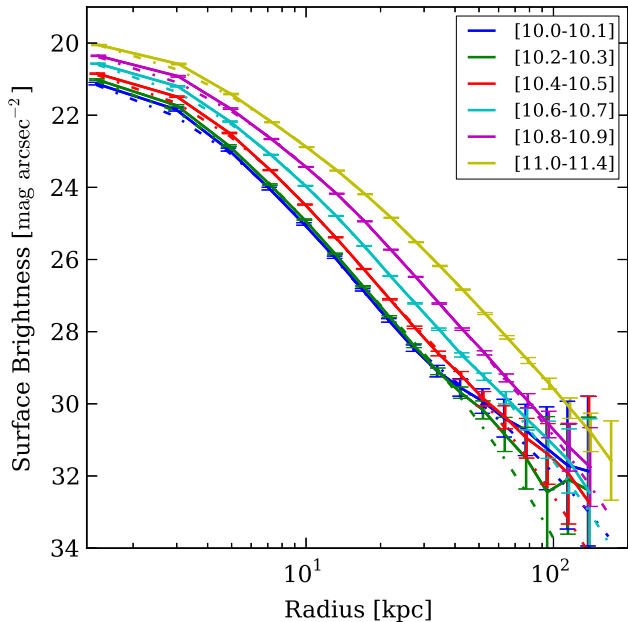


**Figure 11.** We compare the surface brightness profiles of the various stellar mass bins with the double-Sérsic models.

to limited number of galaxy images ( $\sim 1212$ ) which went into the stack. At first glance, our conclusion that a double-Sérsic profile is *always* required may seem surprising, because the surface brightness profiles of massive galaxies with high concentration do not exhibit a clear inflexion point. We note that a single-Sérsic model has a single fixed ellipticity, while the double-Sérsic model with different ellipticities for each component can in a limited way mimic the varying ellipticity of the stacked galaxy image. We investigated whether the change in ellipticity is the dominant factor that favours a double-Sérsic profile over a single-Sérsic profile. To test this, we compare a single-Sérsic and a double-Sérsic profile fitted to similar stacks of galaxies which are not aligned but are randomly oriented. In all cases, the double-Sérsic is still preferred over the single-Sérsic profile. The factor  $2 \log_e(B_{D/S})$  in the randomly oriented case is reduced to one-third of that as calculated in Table 1. This indicates that it is both the surface brightness profile and the ellipticity which contribute to favour a double-Sérsic profile over a single-Sérsic profile.

Plots of the Sérsic indices of the two components as a function of mass are shown in in Figure 12. The outer Sérsic index increases with the mass of the galaxy stack from  $n \sim 3$  to  $n \sim 4$ . The effective radii of each component are also denoted in the Figure 12. The effective radius of the outer component scales as  $\propto 2.5 \log_{10} M_*$  reaching a maximum of 9 kpc for the highest mass bins. We note that the inner Sérsic component is always more elliptical than the outer Sérsic component. The ellipticity of the inner component is approximately constant for all mass bins while the ellipticity of the outer component increases as mass increases.

Having separated the light from the galaxy into two components, we study the variation of the light in the two components as a function of stellar mass. We can also calculate the fraction of light in the outer Sérsic component (Figure 13). We will discuss this result in Section 7.

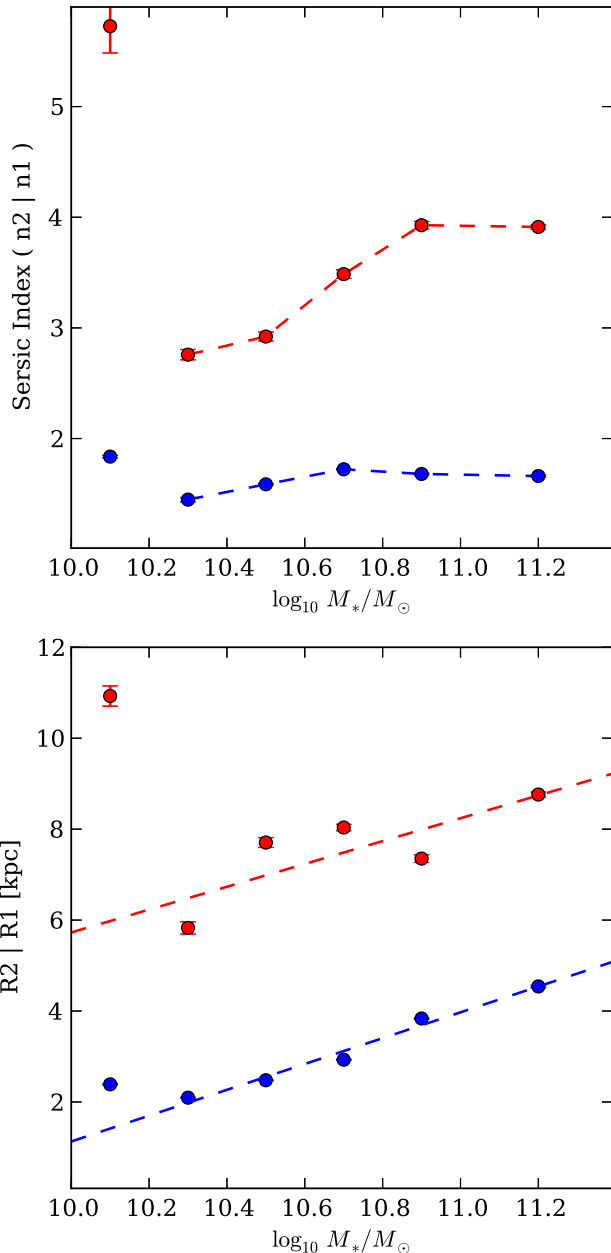


**Figure 12.** (a) The Sérsic indices of the inner(blue) and outer(red) components for high concentration galaxies. (b) The effective radii of the inner(blue) and outer(red) Sérsic components for high concentration galaxies. The outer effective radius scales as  $\propto 2.5 \log_{10} M_*$  while the inner effective radius scales as  $\propto 2.8 \log_{10} M_*$ . The model fails to fit for the lowest mass bin because of insufficient numbers in the stack.

## 5.2 Low Concentration Galaxies

Modelling low concentration galaxies along with their stellar halo component remains a challenging task, because of the extremely low fraction of light in the stellar halo in these systems. Estimates of the stellar halo contribution for M31 lie between 0.6 and 1.5 percent (Ibata et al. 2014), while those for the Milky Way lie between 0.3 and 1.0 percent (Bell et al. 2003; McMillan 2011). Previous modelling and estimates of the stellar halo content of disk galaxies have

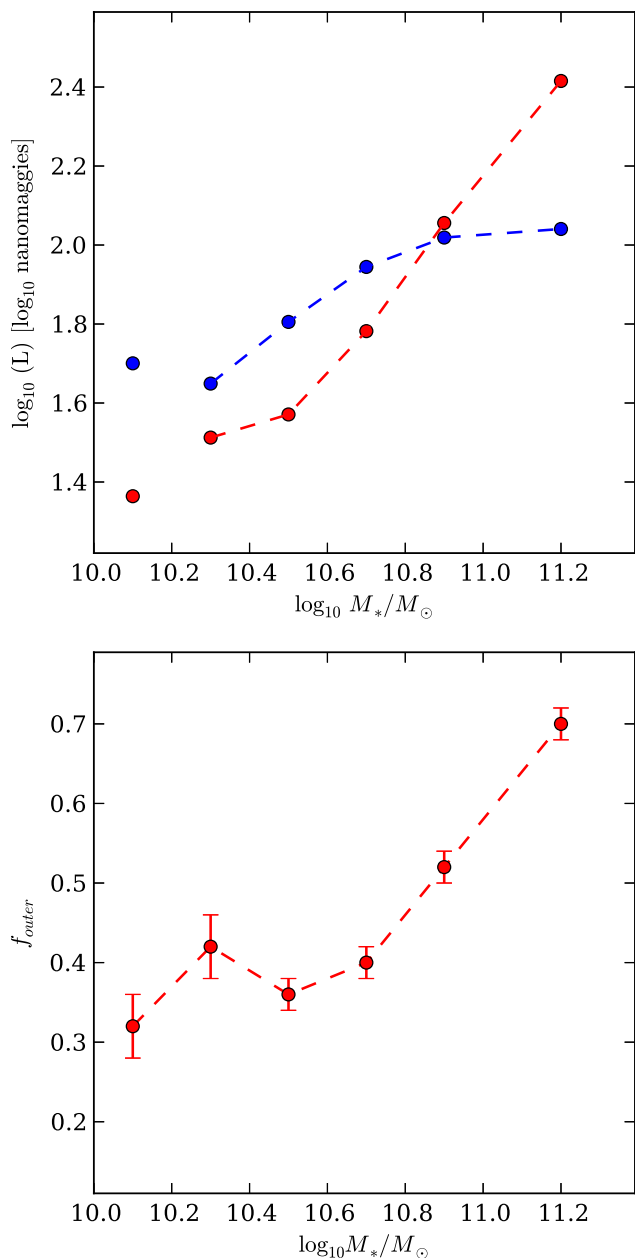


**Figure 13.** (a) The  $\log_{10}$  of the  $r$ -band total Luminosity (in nanomaggies) in the inner (blue) and outer (red) components as a function of stellar mass for high concentration galaxies. (b) The fraction of light in the outer Sérsic component as function of stellar mass for high concentration galaxies.

been made from star counts. In order to detect the stellar halo in face-on disk galaxies, deep imaging is necessary with an accurate determination of the background residuals. Recently van Dokkum et al. (2014) tried to model and determine the stellar halo content of the massive spiral galaxy M101 from integrated surface brightness profiles by going to a depth of  $\mu_g \sim 32$  mag arcsec<sup>-2</sup>. The effective depths of our stacked images are similar to this.

Another important issue is that disk breaks in galaxies (Bakos et al. 2008) also cause inflections in the surface brightness profile of the stacked galaxies and need to be

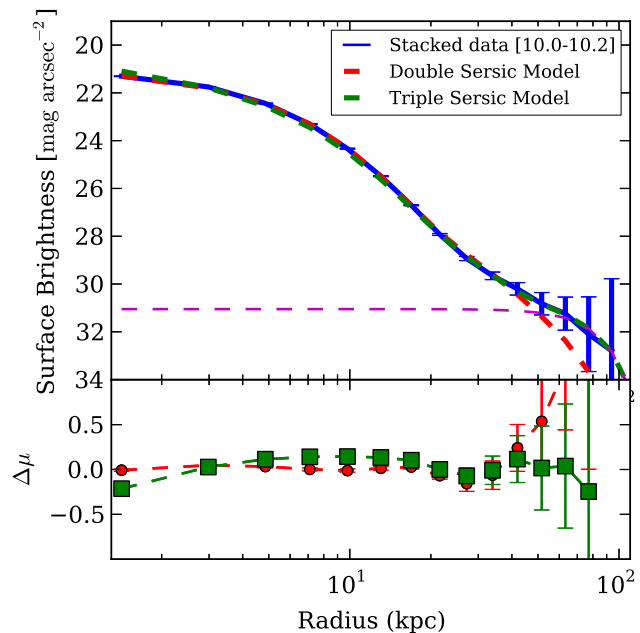


**Figure 14.** The double Sérsic model (shown in red) provides an inadequate fit to low concentration ( $C < 2.6$ ) low mass galaxies ( $10^{10.0}M_\odot < M_* < 10^{10.2}M_\odot$ ). The triple Sérsic model provides a much better fit (shown in green). The third component of the triple Sérsic model is shown in a dashed magenta line. In the bottom panel, the residuals of the double Sérsic model and the triple Sérsic model are shown.

modelled. We find that a double-Sérsic model often fails to fit the stacks of low concentration galaxies, as is shown in Figure 14. In these galaxies, the inflection is caused by disk breaks and these breaks can occur very close to where the stellar halo becomes dominant.

A natural extension of our modelling procedure would be to use a concentric triple Sérsic model. However, the general triple Sérsic model is highly degenerate, especially when trying to separate components which are not easily distinguishable from each other. Face-on disk galaxies with a low stellar-halo mass fraction occupy only a limited parameter space of a three component model. To break these degeneracies, we truncate the inner two components (beyond  $7-8 R_e$ ) and apply restrictions to the third component of the triple Sérsic model. In particular, we look for 3rd component solutions that involve a low Sérsic index ( $n_3 < 1.5$ ), lower effective intensity (in comparison to the other 2 components) and a larger effective radius ( $R_{eff} > 15$  kpc) for the outer-most component. The low Sérsic index ensures that the profile of the third outer component does not rise steeply and dominate the inner central parts of the galaxy.

We also modify our fitting algorithm as follows. We do not fit three components at the same time. We first model independently the galactic disk along with the disk break in high S/N part of the stacked image with a truncated double Sérsic model. Later, having fixed the two components describing the internal part of the galaxy, we add a third component to model the outer extra light. This is necessary because the S/N of the light of the outer image is so much lower than that of the inner regions. If the disk break occurs close to the where the stellar halo becomes dominant (i.e.,

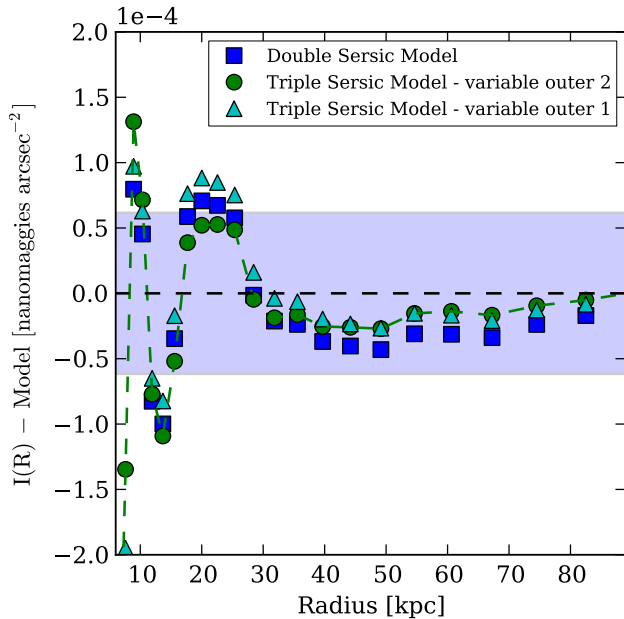


**Figure 15.** The residuals for three models: the double Sérsic, the triple Sérsic by keeping the inner most component fixed (Method A) and the triple Sérsic by keeping the inner two components fixed (Method B) for galaxies stacked in the mass bin range  $10^{10.0}M_{\odot} < M_{*} < 10^{10.2}M_{\odot}$  and with concentration  $C < 2.6$ . The fraction of light of the galaxy in the outermost component by Method A is  $2.3 \pm 0.4\%$  and by method B is  $1.2 \pm 0.3\%$ . The blue band gives the average uncertainty in the background removal for each pixel in  $\text{nanomaggies arcsec}^{-2}$ .

if the stellar halo fraction is not negligible), we first model the internal two components with a truncated double Sérsic model. Then keeping the innermost component fixed, we model the disk break and the extra stellar halo light by fitting two additional Sérsic components. In both methods, we determine the constant sky component at each step.

The global Bayes factor is unable to differentiate between models in the low concentration case, since it is dominated by the asymmetric component (bars, pseudo-bulges, etc.) at the centre of the stacked galaxy. In order to judge which fitting method is most appropriate for a given galaxy stack, we subject every image stack to both methods and calculate the chi-square of the image for each pixel beyond 20 kpc. We compare the reduced chi-square for a double Sérsic model, as well as both methods for determining the third component of the triple Sérsic model, and choose the best fit model. In Figure 15, we compare the residuals of the double Sérsic model as well as the two methods for determining the components of the triple Sérsic model for disk galaxies stacked in the mass bin range  $10^{10.2}M_{\odot} < M_{*} < 10^{10.4}M_{\odot}$ , with concentration index  $C < 2.6$ . The blue band gives the average uncertainty in background removal for each pixel in  $\text{nanomaggies arcsec}^{-2}$ . The procedure which keeps the inner most component fixed and varies the outer two components fares the best. The best fit triple Sérsic model is shown in Figure 14.

The accuracy of modelling the third component depends upon the accuracy of the correct background sky determination. This accuracy is limited by the accuracy of

our background removal. For the model fits to the stack of  $N \sim 3000$  galaxy images shown in Figure 14, if we assume a conservative Sérsic index ( $n \sim 0.4$ ) and an effective radius  $R_e \sim 40$  kpc and an effective magnitude determined by the error of the background residuals ( $I_e \sim 6 \times 10^{-5} \text{ nanomaggies arcsec}^{-2}$ ), the third component can be correctly determined if it is greater than 2% of the total light in the galaxy.

In Figure 16, we plot the fraction of the total light and stellar mass of the galaxy in the inner and outermost components. Results are shown as a function of  $M_{*}$  and for low and high concentration systems. For low concentration galaxies, the higher two mass bins are best fit by double Sérsic models, while the lower mass bins are best fit by triple Sérsic models. Most of the low concentration stacks which are modelled successfully by a triple-Sérsic profile are best fit by keeping only the inner-most component fixed. Only one low concentration stack ( $10^{10.0}M_{\odot} < M_{*} < 10^{10.2}M_{\odot}$ ) could be best fit by fixing the inner two Sérsic components. We will discuss these results later in Section 7.

Improved accuracy in determining the third component may be obtained by stacking a larger number of low concentration galaxies. We stack 12,423 galaxies in the  $r$ -band with random orientations in the mass range  $10^{10.0}M_{\odot} < M_{*} < 10^{10.8}M_{\odot}$ , with a concentration  $C < 2.4$  and with an isophotal axial ratio  $\geq 0.77$ . Using our modelling procedure, we can derive the probability distribution function (PDF) of the fraction of light in the third component (see Figure 17). This fraction is about  $1.3 \pm 0.5\%$ .

Our modelling allows us to identify a radius at which the outer component begins to dominate the integrated stellar light ( $R_{acc}$ ). In Figure 18, the blue squares indicate this radius as a function of  $M_{*}$  for low concentration galaxies. As can be seen, this radius *decreases* as a function of the stellar mass of the galaxy from  $\sim 50$  kpc for galaxies with stellar masses of a few times  $10^{10}M_{\odot}$  to  $\sim 30$  kpc for galaxies with  $M_{*} \sim 10^{11}M_{\odot}$ . For comparison, we also compare  $R_{acc}$  with the radius at which the minimum occurs in the  $g-r$  colour profiles of low concentration galaxies ( $R_{colour\ min}$ ; see Figure 7). The radius at which the outer material begins to dominate is much larger than the radius at which the minimum in the colour profile occurs. This accords well with suggestions in the literature that this minimum in the  $g-r$  colour profile is associated with the break radius in disk galaxies (Bakos et al. 2008).

Also in Figure 18, we compare the radius at which the outer material begins to dominate with the radius at which the  $g-r$  colour profile flattens for high concentration galaxies. The radius at which the  $g-r$  colour profile flattens increases as a function of stellar mass from  $\sim 20$  kpc for galaxies with stellar masses of a few times  $10^{10}M_{\odot}$  to  $\sim 40$  kpc for galaxies with  $M_{*} \sim 10^{11}M_{\odot}$ . The radius at which the outer material begins to dominate is comparatively smaller and decreases as a function of stellar mass. For the highest stellar bin, this radius approaches close to the centre of the galaxy indicating that the outer accreted material is spread all over the galaxy.

## 6 SUMMARY

In this work, we have shown that stacking  $g$  and  $r$  band mosaics of similar galaxies allows us to derive reliable surface

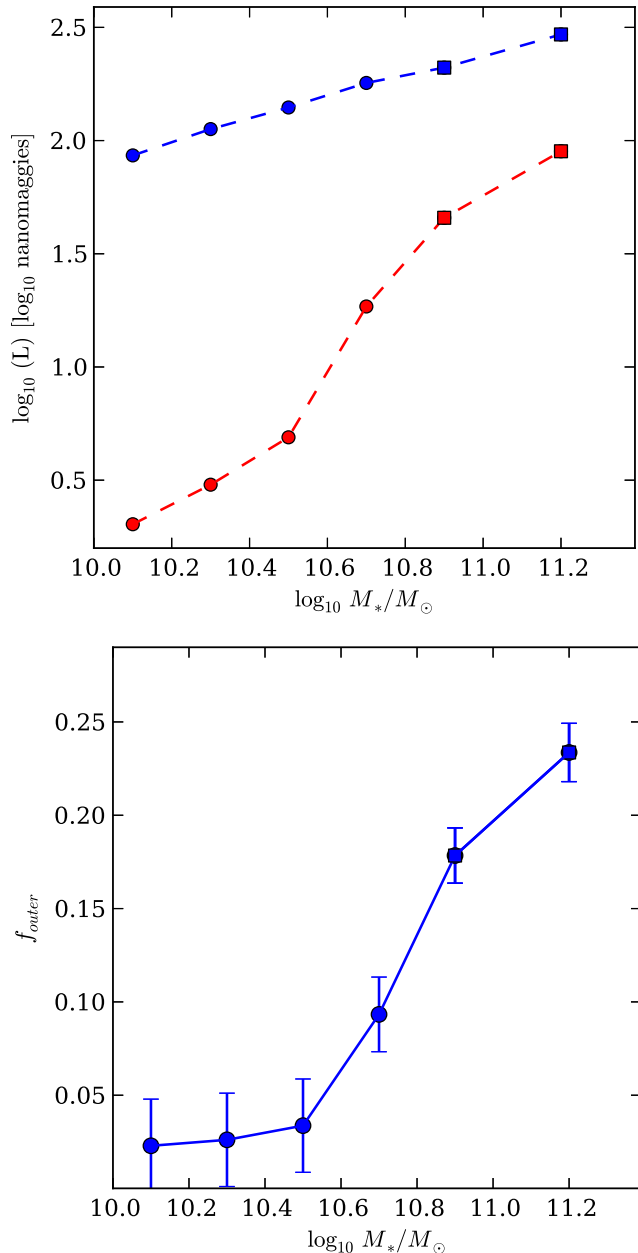


**Figure 16.** (a) The  $\log_{10}$  of the  $r$ -band total luminosity (in nanomaggies) in the inner and outer-most components as a function of stellar mass for low concentration galaxies. (b) The fraction of light in the outer-most Sérsic component as a function of stellar mass for low concentration galaxies. Circular markers indicate that a triple Sérsic profile was required to model the outer parts of the stellar halo, while the square markers indicate that a double Sérsic profile was sufficient.

brightness profiles up to a depth of  $\mu_r \sim 32$  mag arcsec<sup>-2</sup>. We study surface brightness, ellipticity and  $g-r$  colour profiles as a function of stellar mass and galaxy type. We perform fits to the stacked images using multi-component Sérsic models. This enables us to estimate the fraction of the stellar light/mass in the outermost component, which we hypothesize to be built up from accreted stellar material, and to

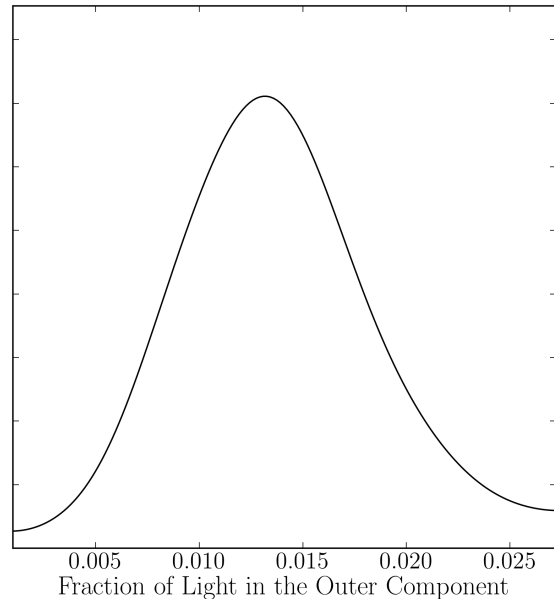


**Figure 17.** The probability distribution function (PDF) of  $f_{outer}$  for the stacked image of disk galaxies in the mass range  $10^{10.0}M_\odot < M_* < 10^{10.8}M_\odot$  and with a concentration of  $C < 2.6$ .

set constraints on theories for the formation of stellar haloes through hierarchical merging.

The main results of this paper can be summarized as follows.

(i) The fraction of accreted stellar material increases with stellar mass. At fixed mass, the fraction of accreted material is higher in early-type than in late-type galaxies.

(ii) The stellar haloes of high concentration galaxies ( $C > 2.6$ ) tend to be more elliptical than those of low concentration galaxies ( $C < 2.6$ ). The ellipticity of the outer stellar halo increases strongly with stellar mass for high concentration galaxies, and more weakly with stellar mass for low concentration galaxies.

(iii) Because we stack galaxies that are nearly face-on, we are only able to probe the colour of the outer accreted component in high concentration galaxies. In these systems, the  $g-r$  colour of the outer halo light is bluer than than the centre of the galaxy and is an increasing function of stellar mass.

(iv) We find that a single-Sérsic profile cannot fit the entire two-dimensional surface brightness distribution of any of our stacked images. Multi-component models are needed to model the excess light in the outer parts of the galaxy, especially between  $\mu_r \sim 28 - 32$  mag arcsec<sup>-2</sup>, and to account for the radial dependence of the ellipticity of the light distribution.

(v) Double-Sérsic profiles adequately model the surface brightness distributions of high concentration galaxies ( $C > 2.6$ ), while triple-Sérsic profiles are often needed to model the surface brightness profile of low concentration galaxies ( $C < 2.6$ ).

(vi) Using the fraction of light in the outer component of our models as a measure of the fraction of the total stellar mass composed of accreted stellar material, we find that this

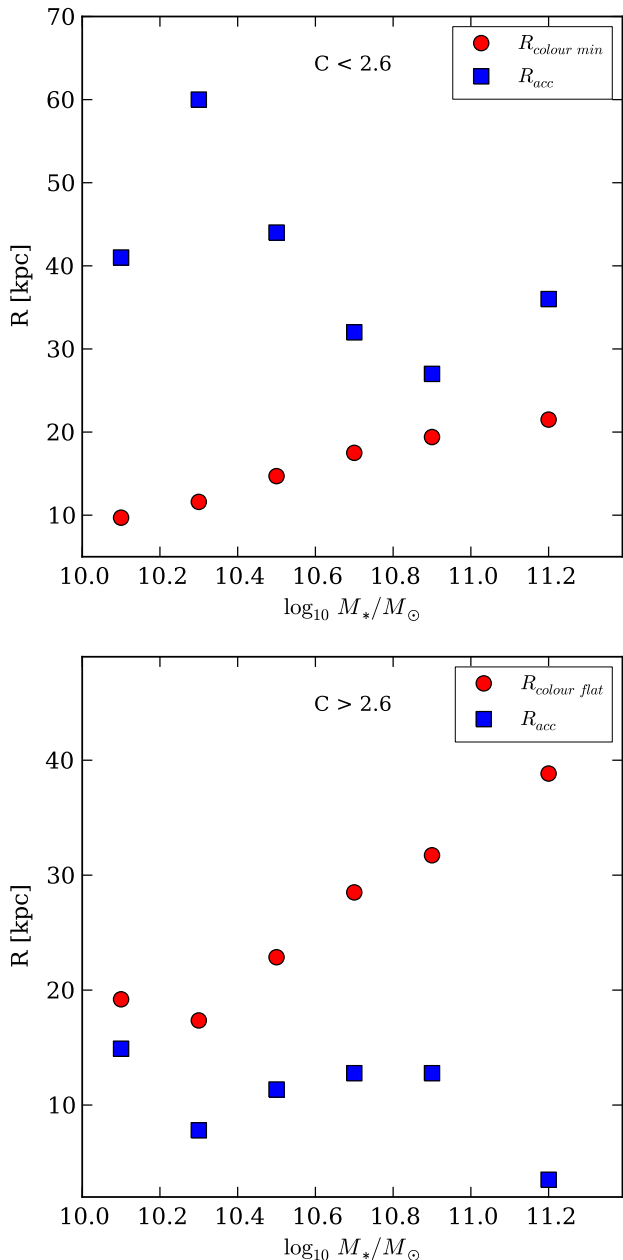


**Figure 18.** (a and b) The radius at which the accreted component begins to dominate over the in-situ component ( $R_{\text{acc}}$ ) for low concentration and high concentration galaxies as a function of stellar mass (blue squares). Also shown is the radius at which there is a minimum in the  $g-r$  colour profiles ( $R_{\text{colour min}}$ ) for low concentration galaxies and the radius at which the  $g-r$  colour profile ( $R_{\text{colour flat}}$ ) flattens for high concentration as a function of stellar mass (red circles).

fraction is an increasing function of stellar mass. At fixed stellar mass, it is also a function of concentration. For high concentration galaxies, the fraction of accreted stellar light rises from 30% to 70%, while for low concentration galaxies the fraction of stellar light rises from 2% to 25% for galaxies in the stellar mass range  $10^{10.0}M_\odot$  to  $10^{11.4}M_\odot$ .

## 7 DISCUSSION

We have attempted to characterise the stellar halo of galaxies through modelling their surface brightness. It is the depth, the large dynamic range and the two-dimensional shape information (ellipticity) of our surface brightness profiles which enables us to recognise deviations from a single component profile and to model successfully the stellar halo of our galaxy stacks out to 100 kpc with two or three components.

An important outcome is that a single Sérsic component cannot fit the surface brightness profiles of high concentration galaxies over a large dynamic range in radius and surface brightness, but can only fit the inner parts of galaxies. The inability of a single Sérsic to fit the two-dimensional surface brightness profile of galaxies has also been confirmed by the studies of Bernardi et al. (2013), Simard et al. (2011) and Lackner & Gunn (2012). Multi-component models are needed to model the full two-dimensional surface brightness profiles of galaxies. We have demonstrated that it is both the average shape of the surface brightness profile and the radial variation in ellipticity of the light in a galaxy stacks that constrain such models.

For high concentration galaxies, the effective radius of the outer component is twice as large as the effective radius of the inner component. For low concentration galaxies, the effective radius of the outer component is much larger than the inner components. For high concentration galaxies, the luminosity of the outer component is a significant fraction of the total luminosity of the galaxy and ranges from 30% to 70%. It also dominates over a large radial range of the galaxy. On the other hand, in low concentration galaxies, the outer component occupies a smaller fraction (from 2% to 25%) and is only dominant at radii larger than 20–30 kpc. In both cases, the fraction of light in the outer component increases with stellar mass (see the red line in the top plots of Figure 16 and Figure 13).

We propose in this work that the fraction of light in the outer component provides a measure of the amount of accreted stellar light in the galaxy. While a direct one-to-one correspondence between the fraction of light in the outer component and the fraction of accreted stellar light cannot be directly proven, the trends in the fraction of light in the outer component agree qualitatively with the trends of the accreted light fraction as a function of mass and galaxy-type in the particle-tagging models of (Cooper et al. 2013). Interestingly, the rate of increase of accreted stellar mass increases dramatically above  $M_* \sim 10^{10.6}M_\odot$ . Interestingly, this corresponds to the stellar mass where galaxies transition from blue/star-forming to red/passive systems (Kauffmann et al. 2003). A significant jump in the accreted mass fraction may be most simply explained by *in-situ* growth of the galaxy being terminated by feedback processes, such as energy injection from relativistic jets produced by black holes in massive galaxies (Croton et al. 2006). In the two stage model of massive galaxy formation proposed by Oser et al. (2010), an early, rapid *in-situ* star formation period is followed by a late merger-dominated period. In the later phase, galaxies tend to grow predominately through minor mergers. We note that the particle tagging models of Cooper et al. (2013) are directly tied to semi-analytic models that include AGN feedback prescription, and thus also include

quenching of *in-situ* growth of galaxies through cooling and star formation. In future work, we intend to undertake a detailed comparison with these models.

Measuring the ellipticity of the outer stellar halo of galaxy also provides us with hints about the formation processes for the stellar halo. A high ellipticity is likely to imply that satellite systems are preferentially accreted along the major axis of the main galaxy (Tal & van Dokkum 2011). The variance in the outer stellar halo profile between different galaxies can be predicted from our surface brightness profiles. This variance results from the fact that similar galaxies can have stellar haloes with very different masses, sizes and shapes. The physical origin of this variance as predicted by the  $\Lambda$ CDM models, is that galaxies of the same mass have had a range of merger histories, resulting in different accreted stellar mass fractions. This has also been clearly demonstrated using particle-tagging techniques on the Aquarius haloes (Cooper et al. 2010), which show very large halo-to-halo differences.

We also note that the integrated surface brightness of the galaxy, including the stellar halo, includes considerably more light than measured by the SDSS `model` and `cModel` magnitudes. For example, for high concentration galaxies in the stellar mass range  $10^{11.0} M_{\odot} < M_{*} < 10^{11.4} M_{\odot}$ , there is about 50% more light contained in the stellar halo at surface brightnesses greater than  $\mu_r \sim 24.5 \text{ mag arcsec}^{-2}$ . This implies that there is considerably more stellar material in the galaxy than one might infer from the SDSS photometry. The stellar masses defined by the MPA-JHU catalogue and used in this work are only used to define the stellar mass bins, and are systematically less than the true stellar mass of the galaxy. This will also be the subject of future work.

## ACKNOWLEDGEMENTS

Funding for SDSS-III has been provided by the Alfred P. Sloan Foundation, the Participating Institutions, the National Science Foundation, and the U.S. Department of Energy Office of Science. The SDSS-III web site is <http://www.sdss3.org/>.

SDSS-III is managed by the Astrophysical Research Consortium for the Participating Institutions of the SDSS-III Collaboration including the University of Arizona, the Brazilian Participation Group, Brookhaven National Laboratory, University of Cambridge, Carnegie Mellon University, University of Florida, the French Participation Group, the German Participation Group, Harvard University, the Instituto de Astrofísica de Canarias, the Michigan State/Notre Dame/JINA Participation Group, Johns Hopkins University, Lawrence Berkeley National Laboratory, Max Planck Institute for Astrophysics, Max Planck Institute for Extraterrestrial Physics, New Mexico State University, New York University, Ohio State University, Pennsylvania State University, University of Portsmouth, Princeton University, the Spanish Participation Group, University of Tokyo, University of Utah, Vanderbilt University, University of Virginia, University of Washington, and Yale University.

## REFERENCES

- Bakos J., Trujillo I., Pohlen M., 2008, *ApJ*, 638, 103  
 Bell E. F., McIntosh D. H., Katz N., & Weinberg M. D. 2003, *ApJS*, 149, 289  
 Bell E. F., Zucker D., Belokurov V. et al. 2008, *ApJ*, 680, 295  
 Bender R., Burstein D., Faber S. M., 1992, *MNRAS*, 399, 462  
 Bergvall N., Zackrisson E., & Caldwell, B. 2010, *MNRAS*, 405, 2697  
 Bernardi M., Meert A., Sheth R. K., Vikram et al. 2013, *MNRAS*, 436, 697  
 Bertin E., & Arnouts S. 1996, *AAPS*, 117, 393  
 Bertin E., Mellier Y., Radovich M., et al. 2002, *ASPC*, 281, 228  
 Blanton M. R., Hogg D. W., Bahcall N. A., et al. 2003, *ApJ*, 592, 819  
 Blanton M. R., Kazin E., Muna D., Weaver B. A., & Price-Whelan, A. 2011, *AJ*, 142, 31  
 Bullock J. S., Johnston K. V., 2005, *ApJ*, 635, 931  
 Croton D. J., Springel V., White S. D. M., De Lucia G., et al. 2006, *MNRAS*, 365, 11  
 Cooper A. P., Cole S., Frenk C. S., White S. D. M., Helly J., Benson A. J., De Lucia G., Helmi A., et al., 2010, *MNRAS*, 406, 744  
 Cooper A. P., D'Souza R., Kauffmann G., et al. 2013, *MNRAS*, 434, 3348  
 Courteau S., Widrow L. M., McDonald M., et al. 2011, *ApJ*, 739, 20  
 de Jong R. S. 2008, *MNRAS*, 388, 1521  
 de Vaucouleurs G., 1948, *Ann d' Astrophys.*, 11, 247  
 de Vaucouleurs G., 1959, *Handbuch Phys.*, 53, 275  
 Feroz F., Hobson M. P., Bridges M. 2008, *MNRAS*, 398, 1601  
 Feroz F., Hobson M. P., Cameron E., & Pettitt A. N. 2013, *arXiv:1306.2144*  
 Fremman K. C., 1970, *AJ*, 160, 811  
 Gonzalez-Perez V., Castander F. J., Kauffmann G. 2011, *MNRAS*, 411, 1151  
 Hubble E. P., 1936, *Realm of the Nebulae*. Yale Univ. Press, New Haven, CT  
 Iбата R. A., Lewis G. F., McConnachie A. W., et al. 2014, *ApJ*, 780, 128  
 Kauffmann G., Heckman T. M., White S. D. M., et al. 2003, *MNRAS*, 341, 33  
 Kauffmann G., Heckman T. M., White S. D. M., et al. 2003, *MNRAS*, 341, 54  
 Kelly B. C., 2007, *ApJ*, 665, 1489  
 Kormendy J. 1977, *ApJ*, 217, 406  
 Kormendy J., Kennicutt R. C. Jr. 2004, *ARA&A*, 42, 603  
 Kormendy J., Fisher D. B., Cornell M. E., Bender R. 2009, *ApJS*, 182, 216  
 Lin H., Flaugher B. & The Dark Energy Survey Collaboration. 2009, *BAAS*, 41, 669  
 Lackner C. N., & Gunn J. E. 2012, *MNRAS*, 421, 2277  
 Lackner C. N., Cen R., Ostriker J. P., Joung M. R. 2012, *MNRAS*, 425, 641  
 LSST Science Collaborations et al., 2009, *preprint* (*arXiv:0912.0201*)  
 Martinez-Delgado D., Gabany R. J., Crawford K. et al. 2010, *AJ*, 140, 962

- Malin D.F., Carter D., 1983, ApJ, 274, 534  
 McGrath E. J., Stockton A., Canalizo G., Iye M., Maihara T., 2008, ApJ, 682, 303  
 McMillan P.J. 2011, MNRAS, 414, 2446  
 Mihos J. C., Harding P., Feldmeier J., Morrison H. 2005, ApJL, 631, L41  
 Monachesi A., Bell E. F., Radburn-Smith D. J., Vlahić et al. 2013, MNRAS, 766, 106  
 Moster B. P., Naab T., White S.D.M., 2013, 428, 3121  
 Oser L., Ostriker J. P., Naab T., Johansson P. H., Burkert A., 2010, ApJ, 725, 2312  
 Peng C. Y., Ho L. C., Impey C. D., & Rix, H.-W. 2010, AJ, 139, 2097  
 Pohlen M., Trujillo I., 2006, A&A, 454, 749  
 Purcell C. W., Bullock J. S., Zentner A. R. 2007, ApJ, 666, 20  
 Schweizer F., 1980, ApJ, 237, 303  
 Schweizer F., Seitzer P., 1992, AJ, 104, 1039  
 Sérsic J. L. 1968, Atlas de Galaxias Australes (Cordoba: Observatorio Astronomico, Univ. Cordoba)  
 Sesar B., Juri M., Ivezi . 2011, ApJ, 2011, 731, 4  
 Schlegel D. J., Finkbeiner D. P., & Davis M. 1998, ApJ, 500, 525  
 Simard L., Mendel J. T., Patton D. R. et al. 2011, ApJS, 196, 11  
 Strateva I., Ivezić Ž., Knapp G. R. 2001, AJ, 122, 1861  
 Suh H., Jeong H., Oh K. et al. 2010, ApJS, 187, 374  
 Tal T., & van Dokkum P. G. 2011, ApJ, 731, 89  
 Tal T., van Dokkum P. G., Nelan J. and Bezanson R. 2009, AJ, 138, 1417  
 Tortora C., Napolitano N. R., Cardone V. F., Capaccioli M., Jetzer Ph., Molinaro, R. 2010, MNRAS, 407, 144  
 van Dokkum P. G., Abraham R., Merritt A. 2014, ApJL, 782, 24  
 Wang W., & White S. D. M. 2012, MNRAS, 424, 2574  
 Yang X., Mo H. J., van den Bosch F. C., et al. 2007, ApJ, 671, 153  
 Zibetti S., White S. D. M., & Brinkmann J. 2004, MNRAS, 347, 556  
 Zibetti S., White S. D. M., Schneider D. P., & Brinkmann J. 2005, MNRAS, 358, 949

## APPENDIX A: THE AMOUNT OF LIGHT MISSED

The masking procedure we have employed is far from perfect. Contamination may arise from the incomplete masking of unresolved sources. An estimate of the amount of light missed as a function of environment can be made by creating mock galaxy images from an appropriate Schechter luminosity function for that environment. For the purpose of estimating how much of unresolved sources is not masked out in our field environment, we generate 1000 realistic mock galaxy  $r$ -band images resembling the field environment of our Sample by using a fixed single Sérsic model for the main central galaxy and the parameters of the  $r$ -band Schechter luminosity function of Blanton et al. (2003) for the galaxy environment. Each galaxy image was convolved with the SDSS  $r$ -band PSF. In addition, Poisson noise was added to each image.

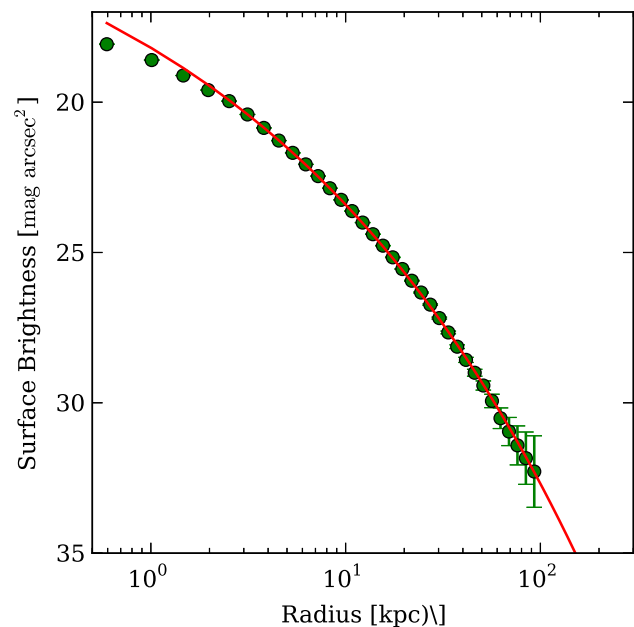


**Figure A1.** Recovered Luminosity Profiles from the mock images. The red line is the initial model convolved with the  $r$ -band PSF.

After subjecting these mocked images to our masking/stacking procedure outlined in the paper, we try to recover the surface brightness profile of the central galaxy. We find that we recover surprisingly well the surface brightness profile over a large range of the galaxy as seen in A1. PSF effects come into play at the centre of the galaxy, while the profile in the faint outer parts depends on the accuracy of the background subtraction.

Our recovery of surface brightness profile can be attributed to a number of factors: First of all, the relatively low density environment of field galaxies help in the masking procedure. Secondly, multiple runs of SExtractor help us to mask out most of the over-lapping galaxies. Thirdly, the percentile cuts we have used in the stacking procedure helps us to deal with failures in the masking procedure especially close to the main galaxy.

## APPENDIX B: MEASUREMENT OF THE OUTER SLOPE

To measure the outer slope ( $m$ ) of the surface brightness profile, we consider a hierarchical Bayesian methodology that takes into consideration measurement errors and the intrinsic scatter in the slope  $\sigma$  (Kelly 2007). Following Equation 2, we can write the likelihood for each measurement  $y_i$  with measurement error  $\delta y_i$  as:

$$p(y_i | \theta) = \frac{1}{\sqrt{2\pi(\delta y_i^2 + \sigma^2)}} \exp \left\{ -\frac{1}{2} \frac{[y_i - E(y_i | \theta)]^2}{\delta y_i^2 + \sigma^2} \right\}, \quad (\text{B1})$$

where  $E(y_i | \theta) = 10^{m \log x_i + c}$ .

Following Kelly (2007), we use uniform priors in  $m$  ( $-10 : 10$ ),  $c$  ( $-100 : 100$ ) and  $\sigma^2$  ( $10^{-8} : 1$ ). We calculate the posterior PDF of each parameter using MULTINEST. For the final parameters, we report the maximum of the

posterior PDF. The uncertainty in the reported parameter is calculated from the variance of the posterior PDF.